

Exact long-range dielectric screening and interatomic force constants in quasi-2D crystals

Miquel Royo¹ and Massimiliano Stengel^{1,2}

¹*Institut de Ciència de Materials de Barcelona (ICMAB-CSIC), Campus UAB, 08193 Bellaterra, Spain**

²*ICREA - Institució Catalana de Recerca i Estudis Avançats, 08010 Barcelona, Spain†*

(Dated: January 22, 2023)

The increasingly vast body of literature on dielectric screening in two-dimensional (2D) crystals has borrowed its founding concepts from the well-known (and long-established) paradigms of the three-dimensional (3D) case: macroscopic potentials are structureless plane waves, and polarizabilities are scalar functions of the wave vector and frequency. Here we show, by performing a rigorous study of the nonanalyticities of the Coulomb kernel in 2D, that neither assumption is *a priori* valid. In particular, we find that the dielectric functions become 2×2 matrices in quasi-2D crystals, with nonuniform macroscopic potentials that are two-component hyperbolic functions of the out-of-plane coordinate, z . This result points to an unexpected *increase* in dimensionality of the screening problem when the spatial dimensionality of the crystal decreases. We demonstrate our arguments by performing a rigorous derivation of the long-range interatomic forces in the adiabatic regime, where we identify a formerly overlooked dipolar coupling involving the out-of-plane components of the dynamical charges. The resulting formula is exact up to an arbitrary multipolar order, which we illustrate in practice via the explicit inclusion of dynamical quadrupoles. By performing numerical tests on monolayer BN, SnS₂ and BaTiO₃ membranes, we show that our method allows for a drastic improvement in the description of the long-range electrostatic interactions, with comparable benefits to the quality of the interpolated phonon band structure.

I. INTRODUCTION

The separation of the interatomic force constants into short-range and long-range contributions has been a mainstay of lattice dynamics theory since the early 50s. [1] The work of Cochran and Cowley [2] has established the correct form of the long-range part in the generic case of an anisotropic three-dimensional (3D) crystal, generalizing the earlier point-charge models. The treatment, however, remained phenomenological until the seminal work of Pick, Cohen and Martin [3], where an analogous formula was derived in the context of first-principles theory, and the acoustic sum rule was formally demonstrated. The advantages of a rigorous derivation are numerous: on one hand, it paved the way for modern first-principles lattice dynamics, within the framework of density-functional perturbation theory; [4–10] on the other hand, it set the stage for further developments in linear-response methods, including higher-order generalizations of the Cochran-Cowley formula. [11, 12]

The interest in lattice-dynamical properties of two-dimensional (2D) crystals has only started relatively recently. As a consequence, in spite of the remarkable progress of the past few years, the corresponding theoretical methods are not as mature as in the 3D case. To understand the nature of the problem (i.e., why traditional algorithms run into trouble in 2D), consider an insulating 2D crystal suspended in vacuum. A phonon propagating at some in-plane wavevector, \mathbf{q} , produces

stray fields that decay asymptotically as $e^{-q|z|}$, where $q = |\mathbf{q}|$ and z is the out-of-plane coordinate. This means that, for a small enough q , the macroscopic electrostatic potential perturbation spreads over a region of space that is much larger than the physical thickness of the material. Such a behaviour complicates the simulation of optical phonons in periodic boundary conditions, as the spurious interaction between repeated images leads to a physically incorrect description of the long-wavelength limit unless special precautions are taken.

To address this issue, the Coulomb cutoff technique [13, 14] is now routinely used in first-principles calculations of phonons [15] and related linear-response properties of suspended 2D systems. Such a treatment cures the pitfalls of a naive supercell-based calculation, and restores the correct physics in the small- q limit by removing the undesired cross-talk between periodically repeated images. For example, the Coulomb cutoff nicely reproduces [15] the physically correct [16] behavior of longitudinal (LO) optical phonons, which are degenerate in frequency with the corresponding transverse (TO) modes right at the Brillouin zone center, and disperse linearly with q in a vicinity of it. [17, 18] Similar issues arise in the calculation of other important materials properties in 2D, ranging from electron-electron [19, 20] and electron-phonon interactions, [21–26] electronic excitations, [27–32] plasmonics [19, 33–36], etc.; in all cases, a sound treatment of the electrostatics is equally crucial as in the lattice-dynamical context.

While the methods to perform the electronic-structure calculations are under control, however, the theory of the long-range electrostatic interactions in two-dimensional crystals is still incomplete. Regarding the interatomic force constants, their long-range contribution has been

* mroyo@icmab.es

† mstengel@icmab.es

inferred by fitting the *ab initio* results to dielectric models, [15] whose general validity remains to be clarified. In other contexts, the description of screening has been oftentimes performed by assuming a strict 2D limit [28], or with the finite thickness of the real crystal heuristically accounted for. [15, 21, 27, 30, 37] Systematic improvement of these models, e.g., along the lines of Ref. 12, appears difficult unless a fundamental first-principles theory of the long-range interactions in *quasi-2D* crystals (that is, by explicitly accounting for the finite physical thickness of the material) is established.

Generalizing the approach of Ref. 3 to the two-dimensional case, however, does not appear as an easy task. In a quasi-2D system the electrostatic interactions are much more complex to understand and describe than in 3D, due to the extreme anisotropy of the physics between the (extended) in-plane and (microscopic) out-of-plane directions. For instance, the usual tenet of 3D electrostatics of representing the macroscopic scalar potentials via structureless plane waves appears inappropriate to the quasi-2D case, where the exponential decay of stray fields in vacuum makes the problem inherently nonuniform along z . This implies, in the language of Ref. 3, that the nonanalyticities of the Coulomb kernel in 2D are not simply restricted to the “head” of the inverse dielectric matrix, but concern an entire *column* of reciprocal-space vectors spanning the out-of-plane direction. Thus, separating long-range from short-range interactions, is *per se* a highly nontrivial issue in 2D, even at the level of the bare kernel (i.e., not considering the additional complications related to screening).

Here we solve the aforementioned challenges by introducing a number of key conceptual and methodological advances. First, we establish a rigorous and general separation between short-range and long-range electrostatic interactions in 2D, both by studying the nonanalytic properties of the Coulomb kernel, and via a physically more intuitive image-charge method. As a direct consequence of such range separation, the macroscopic electrostatic potentials in 2D emerge as two-component hyperbolic functions [$\cosh(qz)$ and $\sinh(qz)$] of the out-of-plane direction, z , reflecting the nonuniform nature of the long-range electrostatic fields. Remarkably, the Dyson equation for the screened Coulomb interaction reduces then to a linear-algebra problem involving 2×2 matrices, i.e., is only marginally more complex than the scalar (1×1) inverse dielectric function that is characteristic of the 3D case. We rationalize this outcome as a manifestation of the inherent *higher dimensionality* of the electrostatics problem in *lower-dimensional* materials: Indeed, the Poisson equation for a phonon traveling in the xy layer plane at some wave vector \mathbf{q} need to be solved in the $\mathbf{q}z$ plane, and is naturally separated into inversion-even and inversion-odd components with respect to $z = 0$. We further show that the lowest-order multipolar expansion of our exact formula recovers the results of the existing dielectric models, but clearly goes beyond them, by (i) identifying a formerly overlooked contribution, i.e., the

interaction between dipoles that are normal to the layer plane; by (ii) generalizing the theory to the next lowest order in \mathbf{q} via incorporation of the dynamical quadrupole tensor; [38] and by (iii) allowing for a more accurate description of the dielectric screening function. Finally, we demonstrate via extensive numerical tests on BN, SnS₂ and BaTiO₃ membranes that our formalism allows for a significant and *systematic* improvement in the existing methods for the theoretical study of phonons in 2D materials. Such an improvement comes at no additional cost from the computational perspective, and only requires a very minor addition to the existing codes.

This work is organized as follows. In Section II A we review the basic concept of range separation in the context of the 3D dielectric matrix formalism of Ref. 3. In Section II B we present our main conceptual achievement, which consists in identifying the nonanalytic part of the Coulomb kernel in quasi-2D systems via an intuitive image-charge construction, and writing it as a 2×2 matrix operator. In Section II C we use these results to establish an exact formula for the long-range part of the force-constants matrix, and provide a simple physical interpretation for the two-component nature of the electrostatics. In Section II D we proceed to the multipolar expansion in powers of \mathbf{q} , and relate the materials-specific parameters to the Born effective charges, macroscopic dielectric tensor and dynamical quadrupoles as calculated within modern DFPT codes; the resulting Eq. (28) is another central achievement of this work. In Section II E we discuss a number of practical issues in achieving an optimal description of the dielectric function and, in parallel, of the long-range force constants. The remainder of this work is dedicated to numerical tests of the formalism, and specifically of its performance in the Fourier interpolation of phonon bands (Sec. III B).

II. THEORY

A. The screened Coulomb interaction

Within the adiabatic approximation, the screened Coulomb interaction W links the screened potential, V^{scr} , to an external charge perturbation, ρ^{ext} , as

$$V^{\text{scr}}(\mathbf{r}) = \int d^3r' W(\mathbf{r}, \mathbf{r}') \rho^{\text{ext}}(\mathbf{r}'). \quad (1)$$

W is, in turn, defined in terms of the bare Coulomb kernel, ν , and the irreducible polarizability χ_{ir} ,

$$W = (\nu^{-1} - \chi_{\text{ir}})^{-1}, \quad (2)$$

where the latter is defined as the (induced) charge response of the interacting electron system to the screened potential. Note that within density-functional approaches χ_{ir} contains the effects of the exchange and correlation kernel, f_{xc} , and can be defined in terms of

the independent-particle polarizability, χ_0 , via a Dyson equation,

$$\chi_{\text{ir}} = \chi_0 + \chi_0 f_{\text{xc}} \chi_{\text{ir}}. \quad (3)$$

The conceptual basis of our method consists in separating the bare Coulomb kernel into a short-range (SR) part and a remainder long-range part,

$$\nu = \nu_{\text{sr}} + \nu_{\text{lr}}. \quad (4)$$

We shall assume that ν_{sr} decays exponentially in real space or, equivalently, can be written as an analytic function of the wavevector \mathbf{q} in reciprocal space; the nonanalytic part of ν is therefore contained in ν_{lr} . We can then define a screened short-range Coulomb interaction,

$$W_{\text{sr}} = (\nu_{\text{sr}}^{-1} - \chi_{\text{ir}})^{-1}, \quad (5)$$

and similarly an intermediate polarizability function, χ_{sr} , where the electrons interact via the exchange-correlation and short-range part of the Coulomb kernel,

$$\begin{aligned} \chi_{\text{sr}} &= \chi_0 + \chi_0 (f_{\text{xc}} + \nu_{\text{sr}}) \chi_{\text{sr}} \\ &= \chi_{\text{ir}} + \chi_{\text{ir}} \nu_{\text{sr}} \chi_{\text{sr}}. \end{aligned} \quad (6)$$

Finally, we define the screened long-range interaction as

$$W_{\text{lr}} = (\nu_{\text{lr}}^{-1} - \chi_{\text{sr}})^{-1}. \quad (7)$$

The rationale consists in reabsorbing the short-range (local fields) part of the Coulomb interactions into the definitions of the SR (intermediate) polarizability, χ_{sr} , and screened interaction, W_{sr} , which are both analytic functions of \mathbf{q} . The effect of the long-range macroscopic electric fields, contained in ν_{lr} , can then be conveniently described in terms of few basic ingredients that are straightforward to calculate.

To see how this strategy works in the specific context of lattice dynamics, we shall follow the dielectric matrix formalism established in Ref. [3]. In our notation, the dynamical matrix can be written as

$$\Phi_{\kappa\alpha, \kappa'\beta} = \rho_{\kappa\alpha}^{\text{ext}} \cdot W \cdot \rho_{\kappa'\beta}^{\text{ext}}, \quad (8)$$

where the external charges refer to the point dipole induced by the displacement of the nuclei. The above definitions naturally lead to a partition of the force-constant matrix into a short-range and a long-range part,

$$\Phi = \Phi^{\text{sr}} + \Phi^{\text{lr}}, \quad (9)$$

$$\Phi_{\kappa\alpha, \kappa'\beta}^{\text{sr}} = \rho_{\kappa\alpha}^{\text{ext}} \cdot W_{\text{sr}} \cdot \rho_{\kappa'\beta}^{\text{ext}}, \quad (10)$$

$$\Phi_{\kappa\alpha, \kappa'\beta}^{\text{lr}} = \rho_{\kappa\alpha}^{\text{sr}} \cdot W_{\text{lr}} \cdot \rho_{\kappa'\beta}^{\text{sr}}, \quad (11)$$

Here $\rho_{\kappa\alpha}^{\text{sr}}$ is the self-consistent charge response to a phonon as calculated within the SR electrostatics,

$$(1 - \chi_{\text{ir}} \nu_{\text{sr}}) \rho_{\kappa\alpha}^{\text{sr}} = \rho_{\kappa\alpha}^{\text{ext}}. \quad (12)$$

	$\varphi - \varphi$	$\varphi - \tau$	$\tau - \tau$	SCF kernel
noninteracting	χ_0			—
irreducible	χ_{ir}			f_{xc}
short-range	χ_{sr}	ρ^{sr}	Φ^{sr}	$f_{\text{xc}} + \nu_{\text{sr}}$
screened	χ	ρ	Φ	$f_{\text{xc}} + \nu$

TABLE I. Summary of the main response functions that we shall consider in this work, together with the SCF kernel that governs the electron-electron interactions in each case. The three central columns refer to the charge response to a scalar potential (χ), the charge response to a phonon (ρ), or the atomic forces induced by a phonon (Φ). [They can all be expressed as second derivatives of the energy with respect to scalar potential (φ) and/or phonon (τ) perturbations.] f_{xc} is the exchange and correlation kernel; ν is the Coulomb kernel; for the meaning of the short-range (sr) label, see text.

Crucially, $\rho_{\kappa\alpha}^{\text{sr}}$ is an analytic function of \mathbf{q} , which means that the material-dependent response functions entering the definition of Φ^{lr} , are all analytic. This property is key in the perspective of an efficient representation of Φ^{lr} , as it allows for a long-wave expansion of both $\rho_{\kappa\alpha}^{\text{sr}}$ and χ_{sr} in a vicinity of the zone center. Typically, only few leading terms need to be retained for an accurate description of the long-range forces, and such quantities are straightforward to calculate within modern implementations of density-functional perturbation theory (DFPT). [9, 10]

In the framework of DFPT, the main response functions discussed in the above paragraphs (see Table I for a summary) can be recast as the second-order variation of the energy with respect to either two scalar potential perturbations (polarizability χ), two phonons (force-constants matrix Φ), or a scalar potential and a phonon (charge response ρ). The various “flavors” of each response function (irreducible, screened, etc.) are then determined by the type of self-consistent (SCF) kernel that is used in the iterative solution of the linear-response problem (right column in Table I). This is particularly convenient, as it avoids the need for explicitly solving the Dyson equations that govern dielectric screening at the microscopic level. Moreover, DFPT methods allow for a more straightforward incorporation of pseudopotentials, which are awkward to treat in the context of the dielectric matrix formalism [e.g., in Eq. (8) and (10) the first-order nuclear potential is that of a point dipole, which implies an all-electron framework].

In three dimensions, the above strategy has been carried out first by Pick, Cohen and Martin in their seminal work [3], by defining as ν_{lr} the $\mathbf{G} = \mathbf{0}$ part of the Coulomb kernel in a vicinity of the zone center. Since the LR kernel is defined by a single Fourier component, both χ_{sr} and $\rho_{\kappa\alpha}^{\text{sr}}$ are scalar functions of the wavevector \mathbf{q} . At the lowest order, we have

$$\chi_{\text{sr}} = -\mathbf{q} \cdot \boldsymbol{\chi} \cdot \mathbf{q} + \dots, \quad (13)$$

$$\rho_{\kappa\alpha}^{\text{sr}} = -i\mathbf{q} \cdot \mathbf{Z}_{\kappa\alpha} + \dots, \quad (14)$$

where $\boldsymbol{\chi}$ and $\mathbf{Z}_{\kappa\alpha}$ are respectively the macroscopic dielectric susceptibility and Born effective charge tensors. (The

dots stand for higher multipolar orders that are usually neglected; a detailed discussion of their significance can be found in Refs. 11 and 12.) We have then, by using Eq. (7),

$$W_{1r} = \left(\frac{q^2}{4\pi} + \mathbf{q} \cdot \boldsymbol{\chi} \cdot \mathbf{q} + \dots \right)^{-1}, \quad (15)$$

which immediately leads, via Eq. (11), to the established formula [3] for the dipole-dipole interaction. The remainder of this work will focus on how this technique can be generalized to systems with reduced dimensionality; in order to do this, we need to seek first of all an appropriate definition of ν_{1r} in 2D.

B. Coulomb kernel in two dimensions

In quasi-2D crystals, it is convenient to separate the total momentum into in-plane ($\mathbf{K}_{\parallel} = \mathbf{G}_{\parallel} + \mathbf{q}$, where \mathbf{G}_{\parallel} belongs to the reciprocal-space Bravais lattice, and \mathbf{q} is the wave vector of the perturbation) and out-of-plane (k_z) components. Then the Coulomb kernel in open boundary conditions can be conveniently written as a function of the in-plane momentum and out-of-plane real-space coordinate z ,

$$\nu(\mathbf{K}_{\parallel}, z - z') = 4\pi \int \frac{dk_z}{2\pi} \frac{e^{ik_z(z-z')}}{K_{\parallel}^2 + k_z^2} = 2\pi \frac{e^{-K_{\parallel}|z-z'|}}{K_{\parallel}}. \quad (16)$$

By analogy with the 3D case, one may be tempted to identify ν_{1r} with the $\mathbf{G}_{\parallel} = 0$ component of Eq. (16), which is clearly nonanalytic. Doing so, however, would be unfit to our purposes: unlike the $\mathbf{G} = 0$ component of the Coulomb kernel in 3D, $\nu(\mathbf{q}, z - z')$ is not a scalar, but an *operator* that depends nontrivially on z and z' . The practical appeal of the range separation method discussed in the previous Section rests on the representability of ν_{1r} in a “small” space, where only one (as in the 3D case) or few physical degrees of freedom of macroscopic character are treated explicitly (see Ref. 39, Chapter 7). Such a condition requires ν_{1r} to be *separable*, i.e., expressible at any given \mathbf{q} as a sum of few terms of the type $\psi_l(z)\xi_l\psi_l(z')$. This is clearly not the case for the function $\nu(\mathbf{q}, z - z')$.

To overcome this obstacle, and thereby achieve a sound separation between short-range and long-range interactions, we shall use the image-charge construction that is illustrated in Fig. 1 (inset). In particular, we shall define the short-range Coulomb kernel as follows,

$$\nu_{sr}(\mathbf{K}_{\parallel}, z - z') = \sum_n (-1)^n \nu(\mathbf{K}_{\parallel}, z - z' - nL). \quad (17)$$

This consists in replacing an external charge perturbation (represented as a red circle with a “+” symbol in Fig. 1) with an infinite array of images, spaced by a distance L along the out-of-plane direction and taken with alternating signs. (We assume that the parameter L is larger

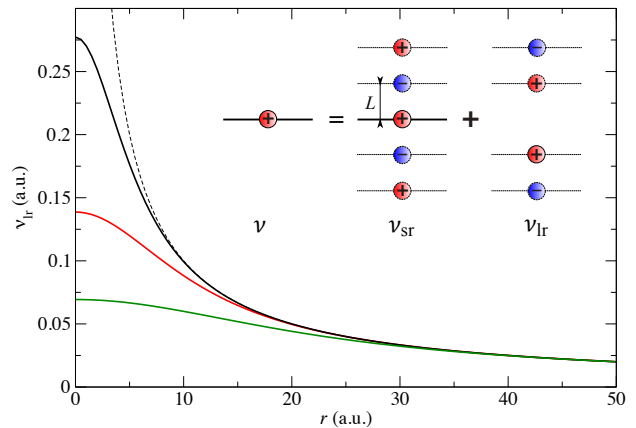


FIG. 1. Real-space representation of the long-range Coulomb kernel as defined in the text. The curves correspond to the choices $L = 5$ a.u. (black), $L = 10$ a.u. (red) and $L = 20$ a.u. (green). The Coulomb potential $1/r$ is shown as a dashed curve for comparison. The inset provides an intuitive illustration of the decomposition of Eq. (17) as an image-charge method.

than the physical thickness of the layer, in such a way that the images do not overlap.) Clearly, the potential produced by a point charge via ν_{sr} is short-ranged (i.e., it vanishes for $r_{\parallel} \gg L$, where r_{\parallel} is the in-plane distance) as the array of images is charge-neutral by construction and has no electrostatic multipoles. Then, the long-range interactions must be entirely contained in ν_{lr} , which is defined via Eq. (4) as the remainder, $\nu_{lr} = \nu - \nu_{sr}$. To illustrate this fact, in the main panel of Fig. 1 we show a real-space representation of ν_{lr} as it results from such a construction. As expected, ν_{lr} deviates significantly from the Coulombic potential only for $r_{\parallel} < L$, where it avoids the $1/r_{\parallel}$ divergence of the latter and tends smoothly to a constant value instead.

The short-range Coulomb kernel as defined in Eq. (17) appears exotic at first sight, so the fact that it has been available for several decades in mainstream implementations of DFPT [40, 41] may come as a surprise to the reader. In a plane-wave electronic-structure code, suspended 2D crystals are routinely calculated by means of the *supercell approach*; this consists in repeating the system periodically along the vacuum direction, while setting the distance between images to some sufficiently large value, L , to avoid any unphysical cross-talk. As we anticipated in the introduction, long-wavelength phonons are problematic to simulate within such a computational setup, as spurious electrostatic interactions between images cannot be avoided in the $\mathbf{q} \rightarrow 0$ limit, unless special precautions (e.g., by means of the Coulomb truncation method) are taken [42]. Such unphysical interactions, however, can be exploited to our advantage, as they provide a straightforward first-principles implementation of Eq. (17). Indeed, a phonon traveling in the superlattice with momentum $(q_x, q_y, q_z = \pi/L)$, i.e., located at

the Brillouin-zone boundary along the vacuum direction, introduces a phase delay of 180° between neighboring images, which reproduces the alternating signs of our image-charge construction. This also implies that our definition of ν_{r} must exactly correspond to the difference between the Coulomb-truncated kernel of Sohler *et al.* and the “zone-boundary” kernel defined above; we shall prove this point in Appendix B. [Interestingly, the Coulomb-truncated kernel can also be understood as an image-charge construction – it only differs from ν_{sr} by a factor e^{-qL} in the odd-numbered terms of Eq. (17).]

An explicit formula for ν_{r} can be derived via a straightforward algebraic manipulation of Eq. (17),

$$\nu_{\text{r}}(\mathbf{K}_{\parallel}, z - z') = \frac{2\pi f(K_{\parallel})}{K_{\parallel}} \cosh[K_{\parallel}(z - z')]. \quad (18)$$

The function $f(K_{\parallel})$ in the prefactor,

$$f(K_{\parallel}) = 1 - \tanh\left(\frac{K_{\parallel}L}{2}\right), \quad (19)$$

is monotonously decreasing, with a linear behavior ($f \simeq 1 - K_{\parallel}L/2$) for small K_{\parallel} , and vanishes exponentially for $K_{\parallel} \gg 1/L$. (For a charge modulation of sufficiently short wavelength, the images do not “see” each other, as the stray fields decay faster than the vacuum thickness. In such a regime, the “zone-boundary” electrostatics coincides with the correct one and ν_{r} , which is defined as the difference, vanishes.) Thus, $f(K_{\parallel})$ can be regarded as a Fourier filter that guarantees smoothness at short distances, while reproducing the slow decay of the Coulombic potential at larger distances. The parameter L defines the length scale of the range separation (see the main panel of Fig. 1), and plays a similar role as the Gaussian width in the well-known Ewald summation method.

One can verify that Eq. (18) exactly reproduces the nonanalytic behavior of the full kernel, Eq. (16), at any order in \mathbf{K}_{\parallel} . To see this, note that both kernels can be written as the same nonanalytic term,

$$\nu_{\text{na}}(\mathbf{K}_{\parallel}, z - z') = \frac{2\pi}{K_{\parallel}} \cosh[K_{\parallel}(z - z')],$$

plus an analytic function of \mathbf{K}_{\parallel} . [In Eq. (16), $e^{-K_{\parallel}|z-z'|} = \cosh(K_{\parallel}|z-z'|) - \sinh(K_{\parallel}|z-z'|)$; both $\tanh\left(\frac{K_{\parallel}L}{2}\right)/K_{\parallel}$ and $\sinh(K_{\parallel}|z-z'|)/K_{\parallel}$ are analytic.]

With these results in hand, we are now ready to attack the representability issue that we raised at the beginning of this Section. At first sight, it might seem that we haven’t made much progress – Eq. (18) is still expressed as a nontrivial function of z and z' . By using the elementary bisection formula of the hyperbolic cosine, however, one can equivalently write Eq. (18) as

$$\nu_{\text{r}}(\mathbf{q}, z - z') = \varphi(z) \cdot \nu_{\text{r}}(\mathbf{q}) \cdot \varphi(z'), \quad (20)$$

in terms of the small-space operator

$$\nu_{\text{r}}(\mathbf{q}) = \frac{2\pi f(q)}{q} \begin{pmatrix} 1 & 0 \\ 0 & -1 \end{pmatrix}, \quad (21)$$

and the two-component macroscopic potential,

$$\varphi(z) = [\cosh(qz), \sinh(qz)]. \quad (22)$$

Eq. (20) now provides the sought-after separable representation of the long-range Coulomb kernel. In spite of the apparent complexity of the electrostatic problem in 2D, with the extreme anisotropy of the physics between the in-plane and out-of-plane directions and the consequent inhomogeneity of the stray fields [here reflected in the nonuniform nature of the macroscopic electrostatic potential, Eq. (22)], we have managed to represent the long-range Coulomb interactions in a space whose dimensionality is only slightly larger than that of the trivial 3D case; we regard this as a remarkable conceptual achievement of this work. We shall demonstrate the implications of this result in the following by incorporating Eq. (20) into the formalism of Sec. II A, which we will use to calculate the screened long-range interatomic forces in 2D.

C. Long-range interatomic forces

In order to write the “lr” part of the dynamical matrix according to Eq. (11) we shall introduce, next to Eq. (21), the small-space representations of the short-range polarizability, $\chi_{\text{sr}}(\mathbf{q})$ (S is the cell surface),

$$\chi_{\text{sr}}^{(lm)}(\mathbf{q}) = \frac{1}{S} \int_{\text{cell}} d^3r \int d^3r' \varphi_l(z) \chi_{\text{sr}}(\mathbf{q}, \mathbf{r}, \mathbf{r}') \varphi_m(z'). \quad (23)$$

and of the charge-density response to a phonon, $\rho_{\kappa\alpha}^{\text{sr}}(\mathbf{q})$,

$$\rho_{\kappa\alpha}^{\text{sr},(m)}(\mathbf{q}) = \int_{\text{cell}} d^3r \rho_{\kappa\alpha}^{\text{sr}}(\mathbf{q}, \mathbf{r}) \varphi_m(z). \quad (24)$$

[The latin indices refer to the hyperbolic cosine and sine components of Eq. (22), respectively.] Note that an explicit calculation of the full polarizability operator, $\chi_{\text{sr}}(\mathbf{q}, \mathbf{r}, \mathbf{r}')$, is not necessary: In the framework of DFPT, the small-space matrix elements of χ_{sr} and ρ^{sr} can be expressed, respectively, as second derivatives of the total energy with respect to two perturbations of the type $\varphi_l(z)$, or with respect to $\varphi_l(z)$ and a phonon. (Charge self-consistency must be treated at the level of the ν_{sr} kernel following the prescriptions of Sec. II A; detailed formulas are provided in Appendix B.) The long-range part of the force-constant matrix reduces then to an elementary linear-algebra problem involving square matrices and vectors of dimension two,

$$\Phi_{\kappa\alpha, \kappa'\beta}^{\text{lr}} = \rho_{\kappa\alpha}^{\text{sr}} \cdot (\nu_{\text{r}}^{-1} - \chi_{\text{sr}})^{-1} \cdot \rho_{\kappa'\beta}^{\text{sr}}. \quad (25)$$

A straightforward calculation of the phonon-phonon response within the same setup then yields the short-range force-constants matrix, Φ^{sr} ; thus, we recover the exact decomposition, Eq. (9), with a computational burden that is essentially the same as a standard calculation of the dynamical matrix.

To understand the physics that lies behind the two-component nature of the electrostatic potentials and operators, it is useful to recall some basic properties of the hyperbolic functions appearing in Eq. (22). The hyperbolic cosine is manifestly an even function of z , while the sine is odd: at the lowest order, the former reduces to an electric field acting parallel to the plane, while the latter corresponds to a perpendicular field. (To reflect this fact, we shall indicate the two components of the relevant matrices and vectors with the “ \parallel ” and “ \perp ” symbols henceforth.) This means that the cosh and sinh potentials mediate electrostatic interactions between charge densities that are, respectively, even and odd with respect to z -reflection. The emergence of an inversion-odd component marks a drastic departure from the 3D case, where transverse electric fields are forbidden by construction as the crystal Hamiltonian retains full translational periodicity in the planes perpendicular to the propagation direction of the phonon.

One may wonder, at this point, whether the cosh and sinh dependence of $\varphi(z)$ carries any deep physical significance beyond its interpretation as a uniform electric field at the leading order in \mathbf{q} . The answer is yes: such a functional dependence has the purpose (a detailed proof can be found in Appendix C) of isolating the *traceless* components of the Cartesian multipole tensor associated with a given charge perturbation. The trace of the Cartesian multipole tensor at any given order, m , is irrelevant for electrostatics, as it does not produce long-range potentials; and the hyperbolic functions enforce this physical fact, demonstrating the internal consistency of our theory. Note that in two dimensions, for $m \geq 1$, there are always *two* independent components of the traceless tensor, corresponding to the cylindrical harmonics in the $\mathbf{q}z$ plane – this is nicely reflected in the two-component nature of the long-range Coulomb interactions as defined by Eq. (21). These harmonics, in turn, can be classified as either inversion-even or inversion-odd with respect to the $z = 0$ axis, consistent with the above arguments. Since the small-space kernel is diagonal in this space, the two subsystems remain uncoupled unless the 2D crystal breaks the $z = 0$ mirror symmetry; we shall see an example shortly.

D. Multipolar expansion

Further insight can be gained by observing that $\cosh(qz)$ and $\sinh(qz)/q$ are both analytic functions of \mathbf{q} , which naturally leads to a long-wave expansion of χ_{sr} and ρ^{sr} . Regarding χ_{sr} , we have

$$\chi_{\text{sr}}(\mathbf{q}) = - \begin{pmatrix} \mathbf{q} \cdot \boldsymbol{\alpha}^{\parallel} \cdot \mathbf{q} & q\boldsymbol{\beta} \cdot \mathbf{q} \\ q\boldsymbol{\beta} \cdot \mathbf{q} & q^2\alpha^{\perp} \end{pmatrix} + O(q^4), \quad (26)$$

where we have introduced the in-plane ($\boldsymbol{\alpha}^{\parallel}$) and out-of-plane (α^{\perp}) macroscopic polarizabilities of the layer, and β_m denotes the off-diagonal elements that couple in-plane and out-of-plane dipoles; their relation to the macroscopic dielectric tensor of the supercell is described in Appendix A. Note that these relationships are *exact*, i.e. they do not rely of any assumption regarding the physical properties of the layer, unlike the dielectric model of Ref. 21.

The charge-response functions, on the other hand, can be conveniently expanded as

$$\rho_{\kappa\alpha}^{\parallel}(\mathbf{q}) = -iq_{\beta} \underbrace{\left[\hat{Z}_{\kappa\alpha}^{(\beta)} - i\frac{q_{\gamma}}{2} \left(\hat{Q}_{\kappa\alpha}^{(\beta\gamma)} - \delta_{\beta\gamma} \hat{Q}_{\kappa\alpha}^{(zz)} \right) + \dots \right]}_{\mathcal{Z}_{\kappa\alpha}^{(\beta)}(\mathbf{q})} e^{-i\mathbf{q} \cdot \boldsymbol{\tau}_{\kappa}}, \quad (27a)$$

$$\rho_{\kappa\alpha}^{\perp}(\mathbf{q}) = q \underbrace{\left[\hat{Z}_{\kappa\alpha}^{(z)} - iq_{\beta} \hat{Q}_{\kappa\alpha}^{(z\beta)} + \dots \right]}_{\mathcal{Z}_{\kappa\alpha}^{\perp}(\mathbf{q})} e^{-i\mathbf{q} \cdot \boldsymbol{\tau}_{\kappa}}, \quad (27b)$$

where the complex phase is a structure factor that depends on the in-plane location of the atom κ within the cell, and we have indicated as $\hat{Z}_{\kappa\alpha}$ and $\hat{Q}_{\kappa\alpha}$ the dynamical dipole and quadrupole tensors in 2D. These generally differ from their standard definitions in 3D (see Appendix A for details): (i) the electrical boundary conditions are set to short circuit in plane, and open circuit along z , consistent with the “zone-boundary” electrostatics; (ii) the Cartesian moments along z are calculated *with respect to the $z = 0$ plane*, which corresponds to the center of the 2D layer. The way $\hat{Q}_{\kappa\alpha}^{(zz)}$ enters Eq. (27), which stems from the asymptotic expansion of the hyperbolic cosine, $\cosh(qz) \simeq 1 + q^2 z^2/2$, is nicely consistent with the traceless nature of the higher-order tensors, which we have anticipated in the previous Section.

While the above formalism is entirely general, for simplicity we shall focus henceforth on 2D crystals that enjoy a mirror plane at $z = 0$. This assumption implies that the off-diagonal component of the polarizability, β_m , vanishes by symmetry, and the diagonal elements of the screened Coulomb interactions can be treated as two separate scalar problems. By plugging the long-wave expansions of the densities, Eq. (27), and the dielectric functions, Eq. (26), into Eq. (25), we obtain the following formula for the long-range interatomic forces,

$$\Phi_{\kappa\alpha, \kappa'\beta}^{\text{lr}}(\mathbf{q}) = \frac{2\pi f(q)}{Sq} \left(\frac{(\mathbf{q} \cdot \boldsymbol{\mathcal{Z}})_{\kappa\alpha}^* (\mathbf{q} \cdot \boldsymbol{\mathcal{Z}})_{\kappa'\beta}}{\epsilon_{\parallel}(\mathbf{q})} - q^2 \frac{\mathcal{Z}_{\kappa\alpha}^{\perp*} \mathcal{Z}_{\kappa'\beta}^{\perp}}{\epsilon_{\perp}(\mathbf{q})} \right) e^{-i\mathbf{q} \cdot (\boldsymbol{\tau}_{\kappa'} - \boldsymbol{\tau}_{\kappa})}. \quad (28)$$

where

$$\epsilon_{\parallel}(\mathbf{q}) = 1 + \frac{2\pi f(q)}{q} \mathbf{q} \cdot (\boldsymbol{\alpha}_{\parallel} + \dots) \cdot \mathbf{q}, \quad (29a)$$

$$\epsilon_{\perp}(\mathbf{q}) = 1 - 2\pi q f(q) (\alpha^{\perp} + \dots). \quad (29b)$$

are the two independent diagonal components of the dielectric function. [Formally, $\epsilon = 1 - \chi\nu$, and relates to the screened Coulomb interaction via $W = \nu\epsilon^{-1}$; the dots stand for the terms $O(q^4)$ and higher in Eq.(26).] \mathcal{Z} are the dynamical dipoles, corresponding to the square brackets in Eq. (27), which generally depend on \mathbf{q} via quadrupolar and higher-order terms. Eq. (28) describes the long-range electrostatic interactions *exactly* up to an arbitrary multipolar order; this is the second central result of this work.

By truncating the expansions of Eq. (26) and Eq. (27) to their leading orders in \mathbf{q} , we recover an *approximate* representation of the long-range force constants that can be directly compared with earlier works on the subject. The inversion-even part of Eq. (28) is consistent with the formula proposed by Sohler *et al.* [15], with the most obvious difference that the Fourier filter $f(q)$ in the prefactor is replaced a Gaussian, $g(q) = e^{-\frac{q^2}{4\lambda}}$, therein. Both functions tend to unity at $\mathbf{q} = 0$ and may therefore appear equivalent at first sight. Our $f(q)$ as given by Eq. (19), however, displays a linear (rather than quadratic) dependence at small q , which is key to reproducing the nonanalytic behavior of the long-range Coulomb kernel exactly. Interestingly, in our formula $f(q)$ also appears in the definition of the dielectric function, Eq. (29); we shall come back to this important point in the following Section.

The inversion-odd part of Eq. (28) is, to the best of our knowledge, an original result of this work. Remarkably, the interaction between out-of-plane dipoles enters with a *negative* sign, which originates from Eq. (21). To rationalize this outcome, note that an unsupported insulating film imposes open-circuit electrical boundary conditions on out-of-plane dipoles, which implies that, at $\mathbf{q} = 0$, optical phonon modes experience a full depolarizing field along z . Such physics is well described by the “zone-boundary” electrostatics that we discussed earlier. When moving away from Γ , the spatial modulation of the dipole moments acts as an effective Yukawa-like *screening*, which progressively weakens the effects of the depolarizing field; the physics is not dissimilar to the driving force towards domain formation in low-dimensional ferroelectrics. As we shall see in the results section, this implies that the ZO branch (optical modes with polarization out of plane) approaches $\mathbf{q} = 0$ with a linear dispersion, similarly to LO modes but with a negative slope. Remarkably, in the inversion-odd component of the dielectric function, Eq. (29), the out-of-plane polarizability of the layer also enters with negative sign, which implies that $\epsilon^{\perp}(\mathbf{q})$ is always smaller than one. This outcome might bear intriguing connections to the theory of negative capacitance [43] effects in thin-film ferroelectrics;

we regard this as a fascinating topic to explore in future studies.

E. The range separation parameter

An interesting outcome of our derivations is that the dielectric function, Eq. (29), explicitly depends on the range separation parameter L via the envelope function $f(q)$. This does not come as a surprise: $\epsilon(\mathbf{q})$ is macroscopic in nature, and therefore only describes the physics of dielectric screening at large distances, i.e., in the regime where the short-range part of the Coulomb kernel is inaccurate. [One could easily incorporate substrate screening effects, e.g., by modifying $\epsilon(\mathbf{q})$ along the guidelines of the Keldysh model. [44]] Consistently, the $f(q)$ prefactor suppresses the polarizability contribution at large momenta, and $\epsilon(\mathbf{q})$ tends to unity for $q \gg L^{-1}$. This observation carries an important message: the dielectric function, $\epsilon(\mathbf{q})$, is generally an ill-defined physical property, as its value at finite momenta depends on the (to a large extent, arbitrary) range L at which we decide to separate “macroscopic” from “local field” effects.

In the case of the inversion-odd component, the progressive suppression of the polarizability contribution for increasing q is not only a natural consequence of the above arguments, but is also an essential ingredient for a mathematically stable description of the long-range interactions. Indeed, the contribution of the layer polarizability α^{\perp} enters with a negative sign, which would lead to a vanishing denominator in Eq. (28) if $f(q)$ were neglected (i.e., set to unity) in Eq. (29). One can show that the stability condition is

$$L > 4\pi\alpha_{\perp}. \quad (30)$$

By recalling the definition of α_{\perp} , Eq. (A4), one quickly realizes that the above condition marks the crossover between a positive and a negative value of ϵ_{zz}^{-1} , the inverse dielectric constant of the hypothetical cell of thickness L that we use to represent our 2D crystal. In other words, assuming a “strict 2D limit” (e.g., following the guidelines of Ref. 28) would be unphysical in the context of the out-of-plane dielectric function: an infinitesimally thin layer with a finite out-of-plane polarizability would inevitably lead to divergencies in the screened Coulomb interaction at short distances.

The above considerations imply that, in practical applications of our formalism, the correct choice of the range-separation parameter L can be important. What remains to be seen is whether there are additional guidelines that one can follow to optimize its value, in addition to the “hard” constraint provided by Eq. (30). To put this question on formal grounds, we shall consider the *screened* counterparts of ρ^{sr} and χ_{sr} (see Sec. II A),

$$\rho_{\kappa\alpha}(\mathbf{q}) = \rho_{\kappa\alpha}^{\text{sr}}(\mathbf{q}) \epsilon^{-1}(\mathbf{q}), \quad (31a)$$

$$\chi(\mathbf{q}) = \chi_{\text{sr}}(\mathbf{q}) \epsilon^{-1}(\mathbf{q}). \quad (31b)$$

The screened functions $\rho_{\kappa\alpha}$ and χ are defined within the Coulomb kernel of the isolated layer, and therefore are independent of the parameter L . In other words, the implicit L -dependence of the “sr” quantities (which originates from the modifications to the short-range Coulomb kernel that a variation of L entails) cancels out *exactly* with an analogous dependence of ϵ when the former are divided by the latter. Such a cancellation becomes only approximate when the multipolar representations of both ρ^{sr} and ϵ are truncated, and such a deviation can be used to gauge the overall accuracy of the method. More specifically, one can define approximate versions of the charge response, polarizability and dielectric functions by plugging the L -independent materials parameters $\hat{\mathbf{Z}}_{\kappa\alpha}$, $\hat{\mathbf{Q}}_{\kappa\alpha}$, α^{\parallel} and α^{\perp} into Eq. (26), Eq. (27) and Eq. (29) while discarding higher-order terms. (We shall indicate such approximate functions with a tilde sign henceforth.) Then, the ratios $\tilde{\rho}_{\kappa\alpha}^{\text{sr}}/\tilde{\epsilon}$ and $\tilde{\chi}^{\text{sr}}/\tilde{\epsilon}$ only depend on L via the $f(q)$ function that is present in the definition of $\tilde{\epsilon}$, which provide a practical means of optimizing L via a comparison to the exact result, Eq. (31).

Such a procedure has the practical disadvantage that it requires an implementation of the macroscopic potential perturbations, $\varphi_l(z)$, in existing linear-response packages. This may be interesting for more sophisticated applications of our formalism, e.g., to the interpolation of electron-phonon matrix elements following the guidelines of Ref. 45. In the context of this work, we have implemented a more straightforward approach of optimizing L , which emerges naturally after incorporating our Eq. (28) into the standard algorithms [12, 15, 46] for the interpolation of the phonon bands. Specifically, one first calculates the full dynamical matrix, Φ , on a discrete mesh (\mathbf{q}_i) spanning the 2D Brillouin zone of the crystal, by using DFPT in conjunction with the Coulomb truncation method. [15, 21] Next, one evaluates the approximate long-range interactions, $\tilde{\Phi}_{\kappa\alpha,\kappa'\beta}^{\text{lr}}(\mathbf{q}_i)$, via the truncated Eq. (28) on the same 2D mesh, and use it to define an approximate short-range part as

$$\tilde{\Phi}^{\text{sr}} = \Phi - \tilde{\Phi}^{\text{lr}}. \quad (32)$$

Finally, $\tilde{\Phi}_{\kappa\alpha,\kappa'\beta}^{\text{sr}}(\mathbf{q}_i)$ is Fourier-interpolated to obtain the short-range dynamical matrix at an arbitrary \mathbf{q} , and eventually the full dynamical matrix once the long-range part $\tilde{\Phi}_{\kappa\alpha,\kappa'\beta}^{\text{lr}}(\mathbf{q})$ is added back to it. Again, $\tilde{\Phi}_{\kappa\alpha,\kappa'\beta}^{\text{lr}}(\mathbf{q})$ only depends on L (the only free parameter) via the envelope function $f(q)$ that is contained in the dielectric functions. To determine the optimal value of L , one can then estimate the decay of the “sr” force constants in real space, and require that it be as fast as possible. This only entails a minimal computational burden, since it only requires recalculating $\tilde{\Phi}_{\kappa\alpha,\kappa'\beta}^{\text{lr}}(\mathbf{q})$ several times at different values of L . This is done at the level of the post-processing program (i.e., it does not imply running additional linear-response calculations); we shall demonstrate this strategy in practice in Section III B.

III. RESULTS

We shall now benchmark the performance of our method regarding the Fourier interpolation of the dynamical matrix elements and eigenvalues (phonon bands). Our computational model consists in the three materials illustrated in Fig. 2, i.e., in two representative 2D monolayer crystals, BN and SnS₂, and a thin membrane of BaTiO₃. (The latter consists in a tetragonal stacking of three BaO/TiO₂/BaO layers, the relaxed structure being non piezoelectric.) To start with, we shall present the calculated physical parameters for our materials set.

A. Calculation of the physical constants

Our calculations are performed within the local-density approximation as implemented in ABINIT [47], by using optimized norm-conserving Vanderbilt pseudopotentials [48] from the PseudoDojo. [49] For all the materials considered, we use a plane-wave cutoff of 80 Hartree and a $12 \times 12 \times 1$ k-point grid. The length of the supercell in the out-of-plane z -direction is set to 40 Bohr in all cases. Before performing the linear-response calculations, we optimize the atomic positions and cell parameters of the unperturbed systems to a stringent tolerance (10^{-8} and 10^{-6} atomic units for residual stress and forces, respectively). The linear-response quantities (dielectric tensor, dynamical charges [46] and quadrupoles [38]) necessary to build the LR dynamical matrix are then computed with the DFPT and longwave drivers of ABINIT [47] and subsequently transformed to the zone-boundary electrostatics following the recipe of Appendix A. The results are reported in Table II.

B. Interpolation of the dynamical matrix

We shall now test the performance of our method regarding the Fourier-interpolation of the phonon bands. In particular, we shall benchmark the results of our in-

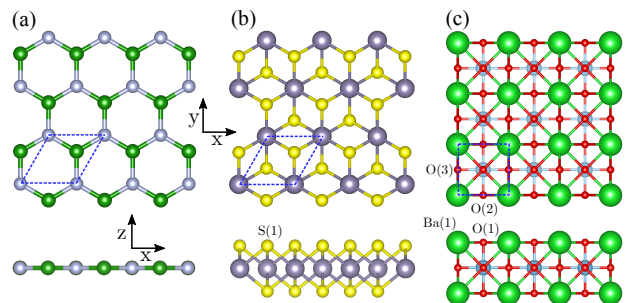


FIG. 2. Atomic structure of the simulated 2D materials: BN (a), SnS₂ (b), BaTiO₃ (c).

	B	N	Sn	S(1)	Ba(1)	Ti	O(1)	O(2)	O(3)
$Z_{\kappa x}^{(x)}$	2.685	-2.685	4.814	-2.407	2.946	6.603	-2.487	-2.285	-5.237
$Z_{\kappa z}^{(z)}$	0.246	-0.246	0.343	-0.171	0.482	0.947	-0.675	-0.280	-0.280
$Q_{\kappa xx}^{(xy)}$	4.261	0.384		3.700					
$Q_{\kappa yy}^{(xx)}$	4.261	0.384		3.700					
$Q_{\kappa yy}^{(yy)}$	-4.261	-0.384		-3.700					
$Q_{\kappa yz}^{(yz)}$				-0.298	1.356		-0.972		
$Q_{\kappa zx}^{(xx)}$				-2.932	-24.552		21.641		
$Q_{\kappa zz}^{(zz)}$				0.231	4.605		-3.868		
α_{\parallel}	1.882		6.629				4.461		
α_{\perp}	0.310		0.720				0.900		

TABLE II. Cartesian components of dynamical dipole, quadrupole and polarizability tensors (in the “zone-boundary” electrostatics). Atomic units are used; only linearly independent coefficients are shown. The numbering of the atoms refers to the convention of Fig. 2.

terpolation method, against the *exact* DFPT phonon frequencies and the frequencies obtained by means of the phenomenological 2D Fourier interpolation of Sohler *et al.* [15] both accessible via the Quantum Espresso [40, 50] (QE) suite. In the course of our tests, we have detected a missing factor of $2\pi/a_0$ in the QE subroutine (version 6.5) that builds the long-range interactions following the guidelines of Ref. [15]. Such a factor likely passed unnoticed in earlier works, [15] as it is close to one (in atomic Bohr units) in all materials studied therein. For a fair comparison, in the following we shall present results obtained *after* having fixed this issue. (Our fix will be incorporated in future releases of the software, presumably starting from v.6.8.)

To calculate the dynamical matrices we use the

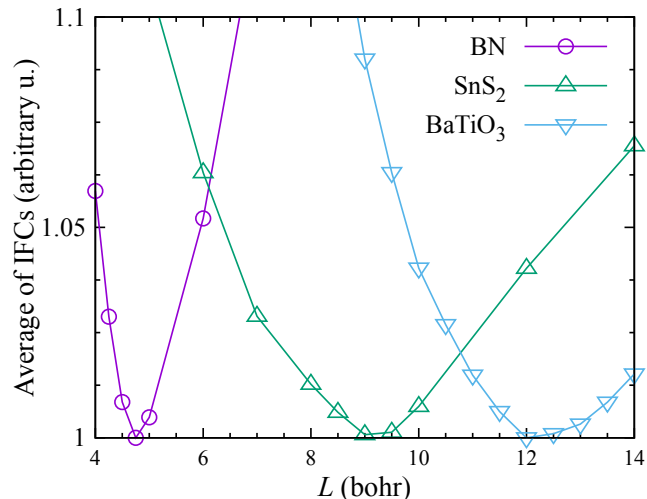


FIG. 3. Average of short-range IFCs (absolute value excluding self-interactions) as a function of the L parameter used to generate the long-range dynamical matrices. For each of the three materials studied in this work the y-axis data have been scaled by the minimum calculated value.

“Coulomb truncation” method [13] as implemented [21, 42] in the linear-response module of QE. For consistency, we use the same computational parameters, exchange and correlation functionals and pseudopotentials as in our ABINIT calculations (see Sec. III A). Prior to performing the actual calculations, we carefully check the compatibility between ABINIT and Quantum Espresso calculations by comparing the main linear-response quantities (polarizabilities and Born effective charges) that can be obtained through both packages, obtaining essentially no differences (within a tolerance of four significant digits).

Once the dynamical matrices are calculated on a grid of in-plane \mathbf{q} points, we follow the procedure described in Sec. II E to perform the interpolation, which we have implemented in an external post-processing module. To determine the optimal value of L , we estimate the accuracy of the interpolation at a given L by summing up the absolute values of the short-range IFCs in real space,

$$d(L) = \sum_{\kappa\kappa'} \sum_l \sum_{\alpha\beta} |\tilde{\Phi}_{\kappa\alpha,\kappa'\beta}^{\text{sr}}(0,l)|, \quad (33)$$

where the prime means that self-interactions are excluded. The minimum of $d(L)$ yields then the sought-after value of L . The results for our tested materials are shown in Fig. 3. For BN, we checked that the value of L optimized via Eq. (33) is consistent with our conclusions based on the analysis of the screened charge, following the guidelines of Sec. II E.

1. BN

We begin by applying our scheme to study the long-wavelength dispersion of the optical phonons in monolayer BN. Phonons in BN have been the subject of several works in the framework of tight-binding models [17], classical potentials [18, 51] or first-principles electronic-structure theory; [15, 52] therefore, this material consti-

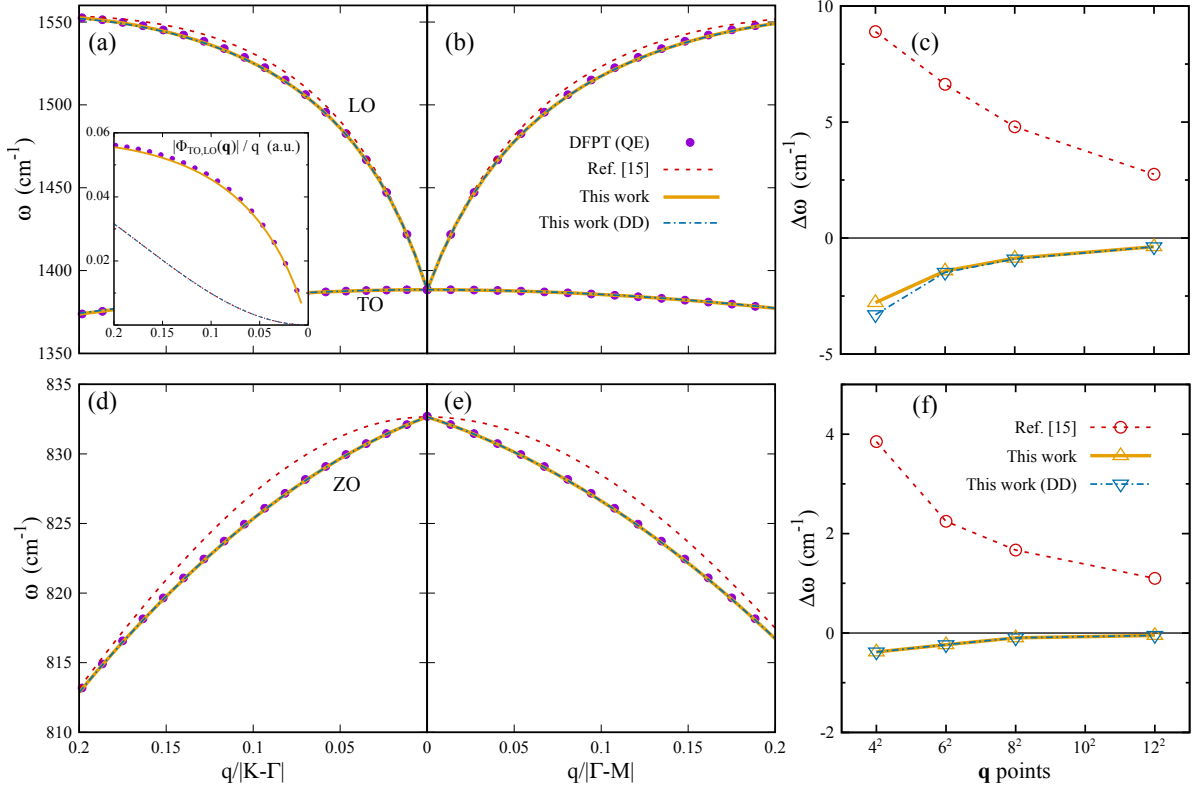


FIG. 4. **BN.** Dispersion of the LO, TO (a–b) and ZO (d–e) phonon branches in the long-wavelength limit along the K– Γ [(a) and (d)] and Γ –M [(b) and (e)] segments in the 2D Brillouin zone. The curves show the results of the 2D Fourier interpolation method of Ref. 15 as implemented in Quantum Espresso after having corrected the bug in the implementation (see text), and of the method developed in this work, either with or without (DD) dynamical quadrupoles; exact [DFPT (QE)] phonon frequencies are shown as circles. All interpolations are performed on a grid of 8×8 in-plane \mathbf{q} points. (c) and (f) show the absolute error resulting from the different interpolation methods as a function of the \mathbf{q} -mesh density for the LO and ZO branches, respectively. DFPT frequencies are taken as reference, and the error is evaluated at the \mathbf{q} point lying halfway between Γ and the first commensurate \mathbf{q} point along the Γ –M segment. The inset in (a) shows the element of the Γ -modes representation of the force-constants matrix [Eq. (34)] that describes the coupling between the TO and LO modes along the K– Γ segment. Absolute values divided by the modulus of \mathbf{q} are represented.

tutes an excellent first benchmark for our method. Fig. 4 shows the results obtained with our Fourier interpolation formalism and using a value of $L = 4.5$ Bohr which, as anticipated in the previous section and confirmed by the data represented in Fig. 3, is optimal in order to minimize the spread of the IFCs. Compared with the bands obtained by following the interpolation of Sohler *et al.*, [15] our method manifestly improves the description of both the LO and ZO branches, accurately reproducing the exact DFPT frequencies.

Regarding the LO mode, we ascribe this improvement to our more accurate treatment of the long-range 2D screening function, while the inclusion of dynamical quadrupoles appears to have a minor impact on the interpolated LO frequencies. To see this, we repeated the interpolation procedure while neglecting dynamical quadrupoles in $\tilde{\Phi}^{\text{lr}}$ (dot-dashed blue curves in Fig. 4), obtaining negligible differences. For a more quantitative comparison, we show in Figs. 4(c) the deviation from the exact LO branch as a function of the \mathbf{q} -mesh resolution:

our method is highly accurate already at a coarse 4×4 mesh, while earlier treatments result in a much slower convergence.

The seemingly negligible impact of the dynamical quadrupoles in the interpolation of the LO frequencies is surprising, so we decided to investigate this point further. We find that the quadrupolar terms are important to reproduce the correct *interactions* between modes, corresponding to the off-diagonal elements of the dynamical matrix, in the long-wavelength limit. To illustrate this point, we project the force-constants matrix at a given wavevector, \mathbf{q} , onto the Γ -point mode eigenvectors ($u_{\kappa\alpha}^m$, m being a mode index), appropriately modulated by a position-dependent complex phase,

$$\Phi_{m,n}(\mathbf{q}) = \langle u_{\kappa\alpha}^m | e^{-i\mathbf{q}\cdot\boldsymbol{\tau}_{\kappa}} \Phi_{\kappa\alpha,\kappa'\beta}(\mathbf{q}) e^{i\mathbf{q}\cdot\boldsymbol{\tau}_{\kappa'}} | u_{\kappa'\beta}^n \rangle. \quad (34)$$

In the inset of Fig. 4(a) we plot the off-diagonal element of $\Phi_{m,n}(\mathbf{q})$, quantifying the strength of the coupling between the LO and TO modes, along a portion of the K– Γ segment. As above, we compare the exact DFPT values

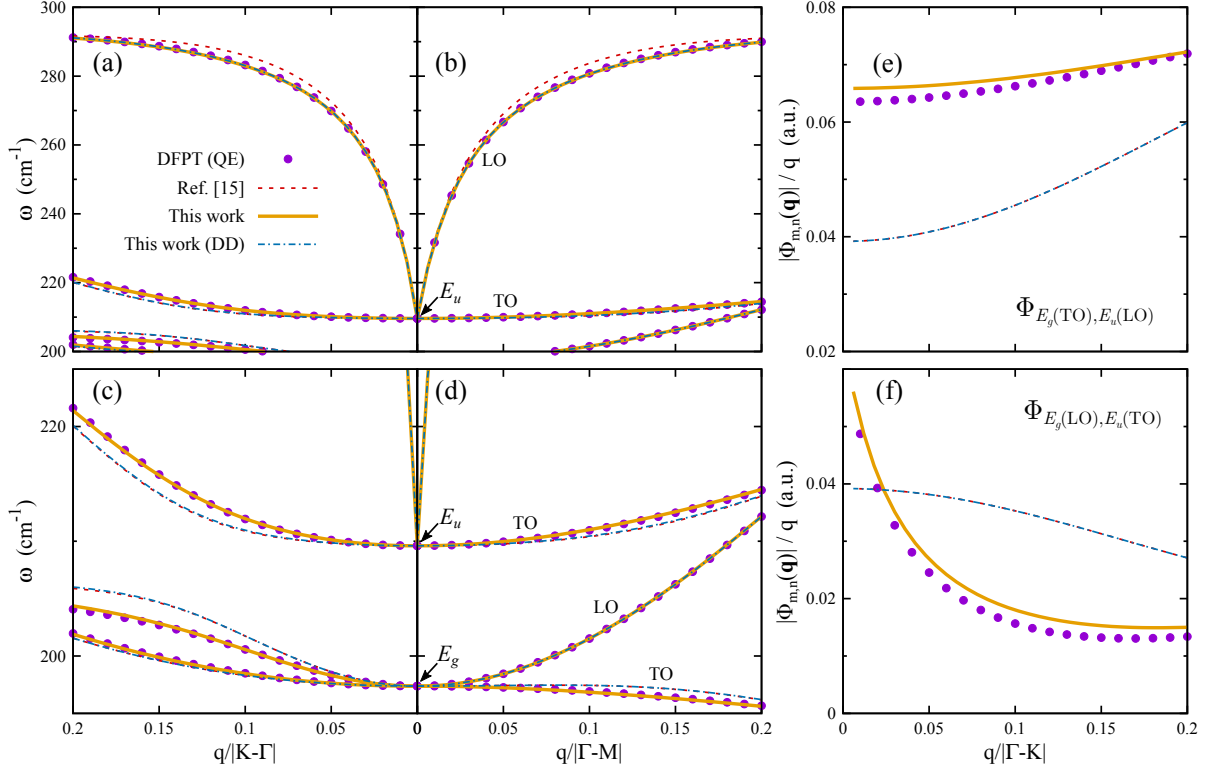


FIG. 5. **SnS₂**. (a-b): Dispersion of the optical E_u branches in the long-wavelength limit along the K- Γ (a) and Γ -M (b) segments in the 2D Brillouin zone. (c-d): Dispersion of the lower-energy E_u and the two E_g branches along the K- Γ (c) and Γ -M (d) segments. Interpolations are performed on a grid of 8×8 in-plane \mathbf{q} points. (e-f): Elements of the Γ -modes representation of the force-constants matrix corresponding to the $E_g(\text{TO})$ - $E_u(\text{LO})$ (e) and $E_g(\text{LO})$ - $E_u(\text{TO})$ (f) couplings along the Γ -K segment. Absolute values divided by $|\mathbf{q}|$ are shown.

with the results of the Fourier interpolation, which we perform either including or excluding the contribution of the dynamical quadrupoles. Clearly, the quadrupoles play a crucial role in ensuring that the long-wave limit is accurately described. Note the qualitative error of the dipole-dipole interpolation, which approaches Γ quadratically instead of linearly. As a matter of fact, the specific treatment of the dipole-dipole terms has no effect on the coupling between these two modes. All the models (except that including the dynamical quadrupoles), or even a complete neglect of the long-range interactions during the interpolation, yield exactly the same result [see inset of Fig. 4(a)].

Regarding the ZO branch of Fig. 4(d-e), note its characteristic linear dispersion when approaching the Γ point, which is reminiscent of the LO branch except for the (negative) sign of the group velocity. This behavior, as we mentioned earlier, stems from the out-of-plane dipole-dipole interactions, which were neglected in earlier works. Indeed, when such interactions are left untreated, as in the dashed curves of Fig. 4(d-e), the Fourier interpolation results a quadratic dispersion, and a discrepancy that decays very slowly with the \mathbf{q} -mesh resolution [Fig. 4(f)]. Our method clearly reproduces the qualitatively correct physics in the long-wavelength limit, with

an excellent match between the interpolated and exact frequencies already at the coarsest mesh resolution that we have considered [Fig. 4(f)]. Note that dynamical quadrupoles are irrelevant here, since their effect on the inversion-odd part of the electrostatics vanishes by symmetry.

2. SnS₂

SnS₂ has been the focus of several studies lately, both in its bulk [53] and monolayer [54] forms. Its main interest lies in the very low lattice thermal conductivity, [55] which is important for thermoelectric efficiency. Clearly, an accurate representation of phonon frequencies is key to these applications, which motivates its consideration as a representative testcase. Note that in the case of SnS₂, a larger (compared to BN) value of $L = 9$ bohr yields an optimally fast decay of the IFCs (see Fig. 3) and has been therefore used in the interpolation.

Fig. 5 shows the dispersion of the four (out of six) optical branches that are lowest in energy. The modes of Fig. 5(a-b) originate from the doubly degenerate E_u mode at the Γ point, with a calculated frequency of $\omega(E_u) = 210$ cm⁻¹, and correspond to the LO and TO

modes with in-plane polarization. Similarly to the BN case, our interpolation scheme has a most visible impact on the highest LO mode, where our improved treatment of screening results in an excellent match with the exact DFPT frequencies. Again, the effect of quadrupoles appears to be unimportant for the interpolation of the LO branch, which is very well described already at the dipole-dipole level.

In Fig. 5(c-d) we show, on a magnified vertical scale, the TO branch of the aforementioned E_u doublet, together with two additional branches deriving from the Raman-active E_g modes [$\omega(E_g) = 197 \text{ cm}^{-1}$]. Here, contrary to the above examples, the inclusion of dynamical quadrupoles is important to reproduce the correct phonon dispersion. This can be clearly appreciated by the comparison with the results of the lower-order models (limited to dipole-dipole interactions), which significantly deviate from the exact DFPT frequencies. The latter, on the other hand, are matched by the full electrostatic model with excellent accuracy.

To understand the reason why the dipole-dipole model is inaccurate for these bands, we have quantified the quadrupolar strength of each mode along the two relevant $\hat{\mathbf{q}}$ -directions, by projecting the calculated components of $Q_{\kappa\alpha}^{(\beta\gamma)}$ on the corresponding Γ -point eigenvectors. Interestingly, the largest discrepancies between the two electrostatic models are observed along the branches where dynamical quadrupoles vanish by symmetry, which might appear counterintuitive at first sight. However, one must keep in mind that Fourier interpolation is a global operation on the 2D Brillouin zone. This means that residual nonanalyticities in the “short-range” dynamical matrix affect the quality of all interpolated branches, including those that are not directly concerned by macroscopic electric fields. It turns out that, similarly to the BN case, the inclusion of dynamical quadrupoles significantly improves the description of the *off-diagonal* matrix elements, which in SnS_2 couple $E_g(\text{TO})$ with $E_u(\text{LO})$ [Fig. 5(e)] and $E_g(\text{LO})$ with $E_u(\text{TO})$ [Fig. 5(f)] when moving away from Γ . Here, the impact on the phonon frequencies is much larger than in BN because the relative closeness in energy of the interacting branches amplifies the effect. We have likewise confirmed that dipole-dipole interactions play no role in interpolating these off-diagonal matrix elements.

Note that two additional optical branches, respectively of A_g and A_u symmetry, are present at higher energies (not shown); the electrostatic corrections, while present, have a relatively lesser impact on their interpolated frequencies.

3. BaTiO_3 membrane

Our motivation for studying a thin perovskite membrane as a showcase for our method stems from the recent surge of interest in such systems. This rapidly growing area of research has been fueled by the experimental

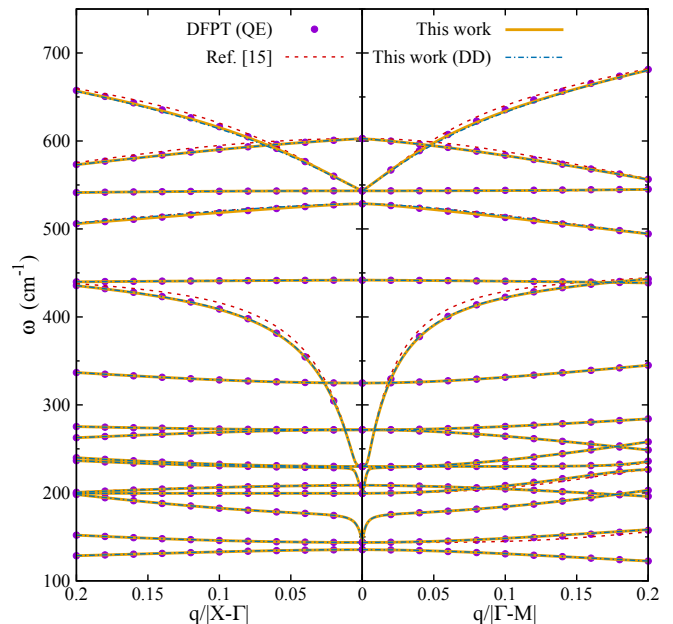


FIG. 6. **BaTiO₃ membrane.** Dispersion of the optical phonon branches in the long-wavelength limit along the X- Γ and Γ -M segments. The interpolated frequencies are obtained from the dynamical matrices calculated on a grid of 8×8 in-plane \mathbf{q} points.

breakthroughs in the preparation of unsupported oxide films via sacrificial layers. [56] The main advantage resides in the unprecedented possibility of studying the impact of reduced size on the properties of perovskite crystals, and on the unprecedented degree of control over the mechanical boundary conditions that a membrane geometry allows. [57] The theoretical study of the phonon spectrum, a mainstay of the current understanding of 3D complex oxides, provides a unique view on the effects of dimensionality on, e.g., the stability of the lattice against a ferroelectric distortion. We shall provide a practical demonstration in the following.

Fig. 6 shows the dispersion of the optical phonons as obtained from the three different interpolation methods that we introduced in the previous paragraphs. We have used an optimal value of $L=12.0$ bohr, once again extracted by minimizing Eq. (33) as shown in Fig. 3. Many of the trends that we have already observed for BN and SnS_2 crystals are manifestly present: i) the highly dispersive LO modes are most affected by the improvements brought about by our new formalism, concretely by the enhanced treatment of screening; ii) the ZO branches exhibit a linear dispersion in long-wavelength limit, requiring explicit treatment of the out-of-plane DD interactions for its qualitatively correct representation; iii) the effect of the dynamical quadrupoles is minimal, and only barely appreciable in the dispersion of the second-highest ZO branch. Interestingly, our interpolation scheme results in an improved description of selected *transverse* optical branches as well. We believe that the discrepancies

produced by the existing scheme might be a “collateral damage” of its inaccurate description of the LO branches: our 2D BaTiO₃ crystal appears to be a case where the small- \mathbf{q} dip in the dispersion of some LO modes is particularly pronounced, possibly affecting the corresponding TO branches as well.

The physical origin of this rather extreme behavior resides in the ferroelectric low-energy mode of BaTiO₃, which is characterized by an abnormally large dipolar strength, Z_l . (Recall that the linear dispersion coefficient of the dynamical matrix eigenvalues close to Γ is proportional to the *square* of Z_l . [15]) Interestingly, the minimal thickness of the film prevents this mode from going “soft” at any point in the 2D Brillouin zone (our centrosymmetric structure is, therefore, at least a metastable configuration of the crystal), pointing to a complete suppression of ferroelectricity in the ultrathin limit. Studying the crossover between 2D and 3D physics as a function of slab thickness in this system will be an exciting topic for future studies. In this perspective, we expect the virtues of our interpolation method to become even more manifest as thickness increases. Indeed, the near-surface dynamical quadrupoles in our scheme grow linearly with thickness because of the dipolar contribution in Eq. (A5), and eventually might become crucially important for a qualitatively correct interpolation.

IV. CONCLUSIONS

In summary, we have developed a rigorous first-principles description of the long-range electrostatic screening and interatomic forces in two-dimensional crystals. As a first application, we have used it to develop an explicit formula, exact up to the quadrupolar order, for the long-range part of the interatomic force constants. Numerical tests on selected materials demonstrate its superior accuracy in the interpolation of the phonon bands, at no extra cost compared to the existing schemes.

Our formalism provides a general platform for treating long-range electrostatics in 2D systems, with an applicability that goes well beyond the specifics of lattice dynamics. For example, one could use it to reconstruct the nonanalytic contributions to the scattering potential in electron-phonon calculations, in a similar spirit as in Refs. 45, 58–60. Next, one could generalize the calculation of the 2D polarizability functions, $\chi(\mathbf{q})$, to finite frequencies, and thereby facilitate the use of modern many-body perturbation techniques in low-dimensional systems. [27, 61] In a materials context, our methods appear well suited to treating emergent systems that lie at the crossover between 2D and 3D, such as oxide membranes, which are attracting a rapidly growing experimental interest. Finally, generalizing our approach to one-dimensional nanowires could be another exciting topic for follow-up studies.

ACKNOWLEDGMENTS

We acknowledge the support of Ministerio de Economía, Industria y Competitividad (MINECO-Spain) through Grants No. MAT2016-77100-C2-2-P, No. PID2019-108573GB-C22 and Severo Ochoa FUNFUTURE center of excellence (CEX2019-000917-S); and of Generalitat de Catalunya (Grant No. 2017 SGR1506). This project has received funding from the European Research Council (ERC) under the European Union’s Horizon 2020 research and innovation program (Grant Agreement No. 724529). Part of the calculations were performed at the Supercomputing Center of Galicia (CESGA).

Appendix A: Dipoles, quadrupoles and polarizabilities in 2D

In the following, we shall discuss how the physical quantities entering Eq.(27) and Eq. (26) are related to the Born dynamical charges ($Z_{\kappa\beta}^{(\alpha)}$), dynamical quadrupoles ($Q_{\kappa\beta}^{(\alpha\gamma)}$) and macroscopic clamped-ion dielectric tensor ($\epsilon_{\alpha\beta}$) that are calculated via the standard linear-response techniques in a supercell geometry. There are two main differences that one needs to take into account: (i) the electrical boundary conditions (EBC) are not the same, since the quantities entering Eq. (26) and Eq. (27) are intended to be calculated within the “zone-boundary” electrostatics, while the standard implementation of Z , Q and ϵ assumes 3D short-circuit boundary conditions (as obtained by removing the nonanalytic $\mathbf{G} = 0$ term from the Coulomb kernel); and (ii) the multipole moments are assumed to be taken with respect to the $z = 0$ symmetry plane, rather than the unperturbed atomic location.

Regarding the Born charges and dielectric polarizabilities, one only needs to worry about (i), since they are both dipolar in character and hence origin-independent. The in-plane Born charges are unaltered by the EBC, i.e. for $\alpha = x, y$ we have

$$\hat{Z}_{\kappa\beta}^{(\alpha)} = Z_{\kappa\beta}^{(\alpha)}. \quad (\text{A1})$$

Conversely, along the out-of-plane direction the so-called “Callen charges” must be used, consistently with the open-circuit EBC that the reference zone-boundary electrostatics imposes along z ,

$$\hat{Z}_{\kappa\beta}^{(z)} = \frac{Z_{\kappa\beta}^{(z)}}{\epsilon_{zz}}. \quad (\text{A2})$$

Regarding the polarizabilities, we can extract the values according to

$$\epsilon_{\alpha\beta} = 1 + 4\pi \frac{\alpha_{\alpha\beta}^{\parallel}}{L}, \quad (\text{A3})$$

$$\epsilon_{zz}^{-1} = 1 - 4\pi \frac{\alpha_{zz}^{\perp}}{L}. \quad (\text{A4})$$

(The indices $\alpha\beta$ run over the two in-plane components.) Note that the parameters $\hat{\mathbf{Z}}_{\kappa\beta}$, α^{\parallel} and α^{\perp} are all independent of the vacuum thickness (provided that the electron density of neighboring images has negligible overlap), as required for well-defined materials properties. The above results are consistent with the prescriptions of Refs. [15, 21, 62]: our work puts them on firmer theoretical grounds, by identifying them with the exact limiting behavior of well-defined response functions.

Devising the conversion rules for the dynamical quadrupoles is slightly more delicate, as different components mix up in a way that is not always intuitive. Regarding the the mixed and out-of-plane components, one has

$$\hat{Q}_{\kappa\beta}^{(z\alpha)} = \frac{Q_{\kappa\beta}^{(z\alpha)} + \tau_{\kappa z} Z_{\kappa\beta}^{(\alpha)}}{\epsilon_{zz}}, \quad (\text{A5a})$$

$$\hat{Q}_{\kappa\beta}^{(zz)} = \frac{Q_{\kappa\beta}^{(zz)} + 2\tau_{\kappa z} Z_{\kappa\beta}^{(z)}}{\epsilon_{zz}}. \quad (\text{A5b})$$

The dielectric constant at the denominator relates to the EBC change, analogously to the above discussion of the Born effective charges. The addition of the Born effective charge times the z coordinate of the atom at the numerator, on the other hand, takes care of the origin shift. Indeed, the dynamical quadrupoles within DFPT can be written as a second moment of the charge density induced by an atomic displacement as [11]

$$Q_{\kappa\beta}^{(\alpha\gamma)} = \int d^3r \rho_{\kappa\beta}(\mathbf{r}) (\mathbf{r} - \boldsymbol{\tau}_{\kappa})_{\alpha} (\mathbf{r} - \boldsymbol{\tau}_{\kappa})_{\gamma}. \quad (\text{A6})$$

One can then break down the z -components of the round brackets as

$$(\mathbf{r} - \boldsymbol{\tau}_{\kappa})_z = z - \tau_{\kappa z}, \quad (\text{A7})$$

and after recalling that the Born charge can also be defined as a real-space moment,

$$Z_{\kappa\beta}^{(\alpha)} = \int d^3r \rho_{\kappa\beta}(\mathbf{r}) (\mathbf{r} - \boldsymbol{\tau}_{\kappa})_{\alpha}, \quad (\text{A8})$$

one quickly arrives at Eq. (A5). We are only left with working out the in-plane components, which can be readily converted as

$$\hat{Q}_{\kappa\beta}^{(\alpha\gamma)} = Q_{\kappa\beta}^{(\alpha\gamma)} - 4\pi\chi_{\alpha\gamma}\hat{Q}_{\kappa\beta}^{(zz)}, \quad (\text{A9})$$

where $\chi_{\alpha\beta}$ are the in-plane components of the macroscopic dielectric susceptibility tensor of the supercell. It is interesting to note that the enforcement of the correct electrical boundary conditions for a suspended 2D layer already endows the in-plane quadrupoles with a contribution from the (zz) component, $\hat{Q}_{\kappa\beta}^{(zz)}$. Because of this, the traceless component that appears in Eq. (27) enjoys a particularly simple expression,

$$\hat{Q}_{\kappa\beta}^{(\alpha\gamma)} - \delta_{\alpha\gamma}\hat{Q}_{\kappa\beta}^{(zz)} = Q_{\kappa\beta}^{(\alpha\gamma)} - \epsilon_{\alpha\gamma}\hat{Q}_{\kappa\beta}^{(zz)}. \quad (\text{A10})$$

One can show that all the components of $\hat{\mathbf{Q}}_{\kappa\beta}$ are all independent of the vacuum thickness, L , unlike those of $\mathbf{Q}_{\kappa\beta}$.

Appendix B: Relationship to the Coulomb cutoff technique

The implementation of the Coulomb cutoff technique follows the prescriptions of Refs. 13, 21, and 42, and consists in writing the open-boundary Coulomb kernel as

$$\nu(\mathbf{K}_{\parallel}, G_n) = \frac{4\pi}{K_{\parallel}^2 + G_n^2} [1 - e^{-K_{\parallel}L} \cos(G_n L)], \quad (\text{B1})$$

where $\mathbf{K}_{\parallel} = \mathbf{G}_{\parallel} + \mathbf{q}$ is an in-plane reciprocal-space vector (\mathbf{G}_{\parallel} spans the Bravais lattice of the primitive 2D cell); G_n form a discrete mesh along z and $L = L_{\text{sc}}/2$ is set to *half* the supercell length in the out-of-plane direction. After observing that $G_n = \frac{\pi n}{L}$, we immediately obtain the following expression for the macroscopic $\mathbf{G}_{\parallel} = 0$ component,

$$\nu(\mathbf{q}, G_n) = \frac{4\pi}{q^2 + G_n^2} [1 - (-1)^n e^{-qL}]. \quad (\text{B2})$$

To link these expressions to the arguments of Section IIB, we shall rewrite the prefactor in the square brackets as follows,

$$[1 - (-1)^n e^{-qL}] = [1 - (-1)^n] + (-1)^n (1 - e^{-qL}) \quad (\text{B3})$$

It is easy to see that the first term on the rhs corresponds to the short-range ‘‘zone-boundary’’ electrostatics,

$$\nu_{\text{sr}}(\mathbf{q}, G_n) = \frac{4\pi}{q^2 + G_n^2} [1 - (-1)^n]. \quad (\text{B4})$$

Indeed, the $[1 - (-1)^n]$ prefactor can be regarded as an implementation of the image-charge method illustrated in Fig. 1. This latter observation reveals that the Coulomb cutoff technique can also be interpreted as an image-charge method: it only differs from ν_{sr} in the prefactor e^{-qL} that scales the negative images, located at odd multiples of L from the $z = 0$ plane. Then, we identify the long-range part of the kernel with the remainder,

$$\nu_{\text{lr}}(\mathbf{q}, G_n) = 4\pi \frac{(-1)^n}{q^2 + G_n^2} (1 - e^{-qL}). \quad (\text{B5})$$

To verify that Eq. (B5) is consistent with the formalism of the earlier sections, recall the following relation for the Fourier series of the hyperbolic cosine function,

$$\int_{-\pi}^{\pi} \cosh(ax) \cos(nx) dx = (-1)^n \frac{2a \sinh(a\pi)}{a^2 + n^2}. \quad (\text{B6})$$

By changing the variable to $z = Lx/\pi$, and by setting $q = \frac{a\pi}{L}$, we have

$$\int_{-L}^L \cosh(qz) \cos(G_n z) dz = (-1)^n \frac{2q \sinh(qL)}{q^2 + G_n^2}. \quad (\text{B7})$$

Then, observe that

$$\sinh(qL) \left[1 - \tanh\left(\frac{qL}{2}\right) \right] = (1 - e^{-qL}). \quad (\text{B8})$$

By combining the above, we eventually obtain

$$\int_{-L}^L \nu_{\text{r}}(\mathbf{q}, z) e^{iG_n z} dz = \nu_{\text{r}}(\mathbf{q}, G_n), \quad (\text{B9})$$

with $\nu_{\text{r}}(\mathbf{q}, z)$ defined as in Eq. (20). The above formulas provide, therefore, the desired representation of the short-range and long-range Coulomb kernels in a supercell context, together with an explicit reciprocal-space expression, Eq. (B7), for the hyperbolic cosine potential of Eq. (22), which can be directly implemented in a first-principles code. (Similar formulas can be easily derived for the inversion-odd component.)

Appendix C: Hyperbolic functions and traceless multipoles

We shall provide a formal demonstration of our statement in Sec.IIC, that the hyperbolic functions consistently pick the traceless component of the first-order charge perturbation at any order in \mathbf{q} . To that end, we shall assume without loss of generality that the x Cartesian axis is aligned with the propagation vector, $\mathbf{q} = (q, 0, 0)$, and write the external charge density perturbation, $\rho^{\text{sr}}(x, z)$, as a two-dimensional function of the real-space coordinates x and z . (z corresponds to the out-of-plane direction; integration over the third trivial direction, y , has already been performed.) The small-space representation of the charge response ρ^{sr} then reads

$$\rho^{\text{sr},(l)}(q) = \int dx \int dz e^{-iqx} \varphi_l(z) \rho^{\text{sr}}(x, z), \quad (\text{C1})$$

where the complex exponential refers to the Fourier transform along x , and $\varphi_l(z)$ stands for the hyperbolic cosine ($l = \parallel$) or sine ($l = \perp$). We can now combine the latter two functions as follows,

$$e^{-iqx} \varphi_l(z) = \frac{e^{q(-ix+z)} \pm e^{q(-ix-z)}}{2}, \quad (\text{C2})$$

where the plus and minus sign refer to cosine and sine, respectively. The expansion of the exponential in powers of q trivially leads to

$$e^{q(-ix+z)} \simeq 1 + q(-ix+z) + \frac{q^2}{2!}(-ix+z)^2 + \dots \quad (\text{C3})$$

If we write the complex number in the round brackets in terms of its modulus, r , times a unitary phase, $e^{i\phi}$, we arrive at

$$e^{q(-ix+z)} = \sum_{n=0}^{\infty} \frac{q^n}{n!} r^n e^{in\phi}. \quad (\text{C4})$$

One can easily recognize the Cartesian representation of the cylindrical harmonics (corresponding to the traceless component of the 2D multipolar tensor), $r^n e^{-in\phi}$, at an arbitrary order n , thereby proving our point.

-
- [1] Max Born and Kun Huang, *Dynamical Theory of Crystal Lattices* (Oxford University Press, Oxford, 1954).
- [2] W. Cochran and R.A. Cowley, “Dielectric constants and lattice vibrations,” *Journal of Physics and Chemistry of Solids* **23**, 447–450 (1962).
- [3] Robert M. Pick, Morrel H. Cohen, and Richard M. Martin, “Microscopic theory of force constants in the adiabatic approximation,” *Phys. Rev. B* **1**, 910–920 (1970).
- [4] NE Zein, “Density functional calculations of crystal elastic modula and phonon-spectra,” *Fiz. Tverd. Tela* **26**, 3028–3034 (1984).
- [5] Stefano Baroni, Paolo Giannozzi, and Andrea Testa, “Green’s-function approach to linear response in solids,” *Phys. Rev. Lett.* **58**, 1861–1864 (1987).
- [6] Xavier Gonze, “Perturbation expansion of variational principles at arbitrary order,” *Phys. Rev. A* **52**, 1086–1095 (1995).
- [7] Xavier Gonze, “Adiabatic density-functional perturbation theory,” *Phys. Rev. A* **52**, 1096–1114 (1995).
- [8] Xavier Gonze, “First-principles responses of solids to atomic displacements and homogeneous electric fields: Implementation of a conjugate-gradient algorithm,” *Phys. Rev. B* **55**, 10337–10354 (1997).
- [9] X. Gonze and C. Lee, “Dynamical matrices, Born effective charges, dielectric permittivity tensors, and interatomic force constants from density-functional perturbation theory,” *Phys. Rev. B* **55**, 10355 (1997).
- [10] S. Baroni, S. de Gironcoli, and A. Dal Corso, “Phonons and related crystal properties from density-functional perturbation theory,” *Rev. Mod. Phys.* **73**, 515 (2001).
- [11] M. Stengel, “Flexoelectricity from density-functional perturbation theory,” *Phys. Rev. B* **88**, 174106 (2013).
- [12] Miquel Royo, Konstanze R. Hahn, and Massimiliano Stengel, “Using high multipolar orders to reconstruct the sound velocity in piezoelectrics from lattice dynamics,” *Phys. Rev. Lett.* **125**, 217602 (2020).
- [13] Sohrab Ismail-Beigi, “Truncation of periodic image interactions for confined systems,” *Phys. Rev. B* **73**, 233103 (2006).
- [14] Carlo A. Rozzi, Daniele Varsano, Andrea Marini, Eberhard K. U. Gross, and Angel Rubio, “Exact Coulomb cutoff technique for supercell calculations,” *Phys. Rev. B* **73**, 205119 (2006).
- [15] Thibault Sohier, Marco Gibertini, Matteo Calandra, Francesco Mauri, and Nicola Marzari, “Breakdown of optical phonons splitting in two-dimensional materials,” *Nano Letters* **17**, 3758–3763 (2017).

- [16] Marta De Luca, Xavier Cartoixa, David I Indolese, Javier Martín-Sánchez, Kenji Watanabe, Takashi Taniguchi, Christian Schönenberger, Rinaldo Trotta, Riccardo Rurali, and Ilaria Zardo, “Experimental demonstration of the suppression of optical phonon splitting in 2D materials by Raman spectroscopy,” *2D Materials* **7**, 035017 (2020).
- [17] D. Sánchez-Portal and E. Hernández, “Vibrational properties of single-wall nanotubes and monolayers of hexagonal BN,” *Phys. Rev. B* **66**, 235415 (2002).
- [18] K. H. Michel and B. Verberck, “Phonon dispersions and piezoelectricity in bulk and multilayers of hexagonal boron nitride,” *Phys. Rev. B* **83**, 115328 (2011).
- [19] Tsuneya Ando, Alan B. Fowler, and Frank Stern, “Electronic properties of two-dimensional systems,” *Rev. Mod. Phys.* **54**, 437–672 (1982).
- [20] Valeri N. Kotov, Bruno Uchoa, Vitor M. Pereira, F. Guinea, and A. H. Castro Neto, “Electron-electron interactions in graphene: Current status and perspectives,” *Rev. Mod. Phys.* **84**, 1067–1125 (2012).
- [21] Thibault Sohier, Matteo Calandra, and Francesco Mauri, “Two-dimensional Fröhlich interaction in transition-metal dichalcogenide monolayers: Theoretical modeling and first-principles calculations,” *Phys. Rev. B* **94**, 085415 (2016).
- [22] Thibault Sohier, Davide Campi, Nicola Marzari, and Marco Gibertini, “Mobility of two-dimensional materials from first principles in an accurate and automated framework,” *Phys. Rev. Materials* **2**, 114010 (2018).
- [23] Wenbin Li, Samuel Poncé, and Feliciano Giustino, “Dimensional crossover in the carrier mobility of two-dimensional semiconductors: The case of InSe,” *Nano Letters* **19**, 1774–1781 (2019).
- [24] Jinlong Ma, Dongwei Xu, Run Hu, and Xiaobing Luo, “Examining two-dimensional Fröhlich model and enhancing the electron mobility of monolayer InSe by dielectric engineering,” *Journal of Applied Physics* **128**, 035107 (2020).
- [25] Samuel Poncé, Wenbin Li, Sven Reichardt, and Feliciano Giustino, “First-principles calculations of charge carrier mobility and conductivity in bulk semiconductors and two-dimensional materials,” *Reports on Progress in Physics* **83**, 036501 (2020).
- [26] Tianqi Deng, Gang Wu, Wen Shi, Zicong Marvin Wong, Jian-Sheng Wang, and Shuo-Wang Yang, “Ab initio dipolar electron-phonon interactions in two-dimensional materials,” arXiv preprint arXiv:2010.02437 (2020).
- [27] Christoph Freysoldt, Philipp Eggert, Patrick Rinke, Arno Schindlmayr, and Matthias Scheffler, “Screening in two dimensions: *GW* calculations for surfaces and thin films using the repeated-slab approach,” *Phys. Rev. B* **77**, 235428 (2008).
- [28] Pierluigi Cudazzo, Ilya V. Tokatly, and Angel Rubio, “Dielectric screening in two-dimensional insulators: Implications for excitonic and impurity states in graphene,” *Phys. Rev. B* **84**, 085406 (2011).
- [29] Timothy C. Berkelbach, Mark S. Hybertsen, and David R. Reichman, “Theory of neutral and charged excitons in monolayer transition metal dichalcogenides,” *Phys. Rev. B* **88**, 045318 (2013).
- [30] S. Latini, T. Olsen, and K. S. Thygesen, “Excitons in van der waals heterostructures: The important role of dielectric screening,” *Phys. Rev. B* **92**, 245123 (2015).
- [31] Ilkka Kylänpää and Hannu-Pekka Komsa, “Binding energies of exciton complexes in transition metal dichalcogenide monolayers and effect of dielectric environment,” *Phys. Rev. B* **92**, 205418 (2015).
- [32] Falco Hüser, Thomas Olsen, and Kristian S. Thygesen, “How dielectric screening in two-dimensional crystals affects the convergence of excited-state calculations: Monolayer MoS₂,” *Phys. Rev. B* **88**, 245309 (2013).
- [33] Jun Yan, Kristian S. Thygesen, and Karsten W. Jacobsen, “Nonlocal screening of plasmons in graphene by semiconducting and metallic substrates: First-principles calculations,” *Phys. Rev. Lett.* **106**, 146803 (2011).
- [34] Kirsten Andersen, Karsten W. Jacobsen, and Kristian S. Thygesen, “Plasmons on the edge of MoS₂ nanostructures,” *Phys. Rev. B* **90**, 161410 (2014).
- [35] Barun Ghosh, Piyush Kumar, Anmol Thakur, Yogesh Singh Chauhan, Somnath Bhowmick, and Amit Agarwal, “Anisotropic plasmons, excitons, and electron energy loss spectroscopy of phosphorene,” *Phys. Rev. B* **96**, 035422 (2017).
- [36] Amit Agarwal, Miriam S Vitiello, Leonardo Viti, Anna Cupolillo, and Antonio Politano, “Plasmonics with two-dimensional semiconductors: from basic research to technological applications,” *Nanoscale* **10**, 8938–8946 (2018).
- [37] Mads L. Trolle, Thomas G. Pedersen, and Valerie Véniard, “Model dielectric function for 2D semiconductors including substrate screening,” *Scientific Reports* **7**, 39844 (2017).
- [38] Miquel Royo and Massimiliano Stengel, “First-principles theory of spatial dispersion: Dynamical quadrupoles and flexoelectricity,” *Phys. Rev. X* **9**, 021050 (2019).
- [39] Richard M Martin, Lucia Reining, and David M Ceperley, *Interacting electrons* (Cambridge University Press, Cambridge, United Kingdom, 2016).
- [40] Paolo Giannozzi, Stefano Baroni, Nicola Bonini, Matteo Calandra, Roberto Car, Carlo Cavazzoni, Davide Ceresoli, Guido L Chiarotti, Matteo Cococcioni, Ismaila Dabo, Andrea Dal Corso, Stefano de Gironcoli, Stefano Fabris, Guido Fratesi, Ralph Gebauer, Uwe Gerstmann, Christos Gougoussis, Anton Kokalj, Michele Lazzeri, Layla Martin-Samos, Nicola Marzari, Francesco Mauri, Riccardo Mazzarello, Stefano Paolini, Alfredo Pasquarello, Lorenzo Paulatto, Carlo Sbraccia, Sandro Scandolo, Gabriele Sclauzero, Ari P Seitsonen, Alexander Smogunov, Paolo Umari, and Renata M Wentzcovitch, “QUANTUM ESPRESSO: a modular and open-source software project for quantum simulations of materials,” *Journal of Physics: Condensed Matter* **21**, 395502 (2009).
- [41] X. Gonze, B. Amadon, P.-M. Anglade, J.-M. Beuken, F. Bottin, P. Boulanger, F. Bruneval, D. Caliste, R. Caracas, M. Côté, T. Deutsch, L. Genovese, Ph. Ghosez, M. Giantomassi, S. Goedecker, D.R. Hamann, P. Hermet, F. Jollet, G. Jomard, S. Leroux, M. Mancini, S. Mazevet, M.J.T. Oliveira, G. Onida, Y. Pouillon, T. Rangel, G.-M. Rignanese, D. Sangalli, R. Shaltaf, M. Torrent, M.J. Verstraete, G. Zerah, and J.W. Zwanziger, “ABINIT: First-principles approach to material and nanosystem properties,” *Computer Phys. Commun.* **180**, 2582–2615 (2009).
- [42] Thibault Sohier, Matteo Calandra, and Francesco Mauri, “Density functional perturbation theory for gated two-dimensional heterostructures: Theoretical developments and application to flexural phonons in graphene,” *Phys. Rev. B* **96**, 075448 (2017).

- [43] Pavlo Zubko, Jacek C Wojdeł, Marios Hadjimichael, Stéphanie Fernandez-Pena, Anaïs Sené, Igor Luk'yanchuk, Jean-Marc Triscone, and Jorge Íñiguez, "Negative capacitance in multidomain ferroelectric superlattices," *Nature* **534**, 524–528 (2016).
- [44] LV Keldysh, "Coulomb interaction in thin semiconductor and semimetal films," *Soviet Journal of Experimental and Theoretical Physics Letters* **29**, 658 (1979).
- [45] Guillaume Brunin, Henrique Pereira Coutada Miranda, Matteo Giantomassi, Miquel Royo, Massimiliano Stengel, Matthieu J. Verstraete, Xavier Gonze, Gian-Marco Rignanese, and Geoffroy Hautier, "Electron-phonon beyond Fröhlich: Dynamical quadrupoles in polar and covalent solids," *Phys. Rev. Lett.* **125**, 136601 (2020).
- [46] X. Gonze and C. Lee, "Dynamical matrices, Born effective charges, dielectric permittivity tensors, and interatomic force constants from density-functional perturbation theory," *Phys. Rev. B* **55**, 10355 (1997).
- [47] Aldo H. Romero, Douglas C. Allan, Bernard Amadon, Gabriel Antonius, Thomas Applencourt, Lucas Baguet, Jordan Bieder, François Bottin, Johann Bouchet, Eric Bousquet, Fabien Bruneval, Guillaume Brunin, Damien Caliste, Michel Côté, Jules Denier, Cyrus Dreyer, Philippe Ghosez, Matteo Giantomassi, Yannick Gillet, Olivier Gingras, Donald R. Hamann, Geoffroy Hautier, François Jollet, Gérard Jomard, Alexandre Martin, Henrique P. C. Miranda, Francesco Naccarato, Guido Petretto, Nicholas A. Pike, Valentin Planes, Sergei Prokhorenko, Tonatiah Rangel, Fabio Ricci, Gian-Marco Rignanese, Miquel Royo, Massimiliano Stengel, Marc Torrent, Michiel J. van Setten, Benoit Van Troeye, Matthieu J. Verstraete, Julia Wiktor, Josef W. Zwanziger, and Xavier Gonze, "ABINIT: Overview and focus on selected capabilities," *The Journal of Chemical Physics* **152**, 124102 (2020).
- [48] D. R. Hamann, "Optimized norm-conserving Vanderbilt pseudopotentials," *Phys. Rev. B* **88**, 085117 (2013).
- [49] M.J. van Setten, M. Giantomassi, E. Bousquet, M.J. Verstraete, D.R. Hamann, X. Gonze, and G.-M. Rignanese, "The PseudoDojo: Training and grading a 85 element optimized norm-conserving pseudopotential table," *Computer Physics Communications* **226**, 39–54 (2018).
- [50] P Giannozzi, O Andreussi, T Brumme, O Bunau, M Buongiorno Nardelli, M Calandra, R Car, C Cavazzoni, D Ceresoli, M Cococcioni, N Colonna, I Carnimeo, A Dal Corso, S de Gironcoli, P Delugas, R A DiStasio, A Ferretti, A Floris, G Fratesi, G Fugallo, R Gebauer, U Gerstmann, F Giustino, T Gorni, J Jia, M Kawamura, H-Y Ko, A Kokalj, E Küçükbenli, M Lazzeri, M Marsili, N Marzari, F Mauri, N L Nguyen, H-V Nguyen, A Otero de-la Roza, L Paulatto, S Poncé, D Rocca, R Sabatini, B Santra, M Schlipf, A P Seitsonen, A Smogunov, I Timrov, T Thonhauser, P Umari, N Vast, X Wu, and S Baroni, "Advanced capabilities for materials modelling with quantum ESPRESSO," *Journal of Physics: Condensed Matter* **29**, 465901 (2017).
- [51] Jin-Wu Jiang, Bing-Shen Wang, and Harold S. Park, "Topologically protected interface phonons in two-dimensional nanomaterials: hexagonal boron nitride and silicon carbide," *Nanoscale* **10**, 13913–13923 (2018).
- [52] Ludger Wirtz, Angel Rubio, Raul Arenal de la Concha, and Annick Loiseau, "Ab initio calculations of the lattice dynamics of boron nitride nanotubes," *Phys. Rev. B* **68**, 045425 (2003).
- [53] Zhi-Qiang Zhen and Hai-Yan Wang, "Density functional study of the electronic, elastic, and lattice dynamic properties of SnS₂," *Acta Physica Polonica, A* **137** (2020).
- [54] Aamir Shafique, Abdus Samad, and Young-Han Shin, "Ultra low lattice thermal conductivity and high carrier mobility of monolayer SnS₂ and SnSe₂: a first principles study," *Physical Chemistry Chemical Physics* **19**, 20677–20683 (2017).
- [55] Wenke He, Dongyang Wang, Jin-Feng Dong, Yang Qiu, Liangwei Fu, Yue Feng, Yujie Hao, Guangtao Wang, Jinfeng Wang, Chang Liu, *et al.*, "Remarkable electron and phonon band structures lead to a high thermoelectric performance $ZT > 1$ in earth-abundant and eco-friendly SnS crystals," *Journal of Materials Chemistry A* **6**, 10048–10056 (2018).
- [56] Di Lu, David J Baek, Seung Sae Hong, Lena F Kourkoutis, Yasuyuki Hikita, and Harold Y Hwang, "Synthesis of freestanding single-crystal perovskite films and heterostructures by etching of sacrificial water-soluble layers," *Nature Materials* **15**, 1255–1260 (2016).
- [57] Seung Sae Hong, Mingqiang Gu, Manish Verma, Varun Harbola, Bai Yang Wang, Di Lu, Arturas Vailionis, Yasuyuki Hikita, Rossitza Pentcheva, James M. Rondinelli, and Harold Y. Hwang, "Extreme tensile strain states in La_{0.7}Ca_{0.3}MnO₃ membranes," *Science* **368**, 71–76 (2020).
- [58] Guillaume Brunin, Henrique Pereira Coutada Miranda, Matteo Giantomassi, Miquel Royo, Massimiliano Stengel, Matthieu J. Verstraete, Xavier Gonze, Gian-Marco Rignanese, and Geoffroy Hautier, "Phonon-limited electron mobility in Si, GaAs, and GaP with exact treatment of dynamical quadrupoles," *Phys. Rev. B* **102**, 094308 (2020).
- [59] Vatsal A. Jhalani, Jin-Jian Zhou, Jinsoo Park, Cyrus E. Dreyer, and Marco Bernardi, "Piezoelectric electron-phonon interaction from ab initio dynamical quadrupoles: Impact on charge transport in wurtzite GaN," *Phys. Rev. Lett.* **125**, 136602 (2020).
- [60] Jinsoo Park, Jin-Jian Zhou, Vatsal A. Jhalani, Cyrus E. Dreyer, and Marco Bernardi, "Long-range quadrupole electron-phonon interaction from first principles," *Phys. Rev. B* **102**, 125203 (2020).
- [61] H Felipe, Lede Xian, Angel Rubio, and Steven G Louie, "Universal slow plasmons and giant field enhancement in atomically thin quasi-two-dimensional metals," *Nature communications* **11**, 1–10 (2020).
- [62] Tian Tian, Declan Scullion, Dale Hughes, Lu Hua Li, Chih-Jen Shih, Jonathan Coleman, Manish Chhowalla, and Elton J. G. Santos, "Electronic polarizability as the fundamental variable in the dielectric properties of two-dimensional materials," *Nano Letters* **20**, 841–851 (2020).